

Gapless quantum spin liquid ground state in mixed-valence iridate $\text{Ba}_3\text{InIr}_2\text{O}_9$

Tusharkanti Dey,^{1,*} M. Majumder,¹ J. C. Orain,² A. Senyshyn,³ M. Prinz-Zwick,⁴
F. Bert,⁵ P. Khuntia,⁵ N. Büttgen,⁴ A. A. Tsirlin,^{1,†} and P. Gegenwart^{1,‡}

¹*Experimental Physics VI, Center for Electronic Correlations and Magnetism,
University of Augsburg, 86159 Augsburg, Germany*

²*Laboratory for Muon Spin Spectroscopy, Paul Scherrer Institut, 5232 Villigen PSI, Switzerland*

³*Forschungszentrum für Neutronenphysik und Materialforschung (FRM II),
Technische Universität München, 85747 Garching, Germany*

⁴*Experimental Physics V, Center for Electronic Correlations and Magnetism,
University of Augsburg, 86159 Augsburg, Germany*

⁵*Laboratoire de Physique des Solides, CNRS, Univ. Paris-Sud,
Université Paris-Saclay, 91405 Orsay Cedex, France*

Using thermodynamic measurements, neutron diffraction, nuclear magnetic resonance, and muon spin relaxation, we establish quantum spin liquid behavior in the structurally perfect iridate $\text{Ba}_3\text{InIr}_2\text{O}_9$, where unpaired electrons are localized on the Ir_2O_9 dimers with the mixed-valence $\text{Ir}^{4.5+}$ ions. Despite the antiferromagnetic Curie-Weiss temperature on the order of 10 K, neither long-range magnetic order nor spin freezing are observed down to 20 mK, such that spins are short-range-correlated and dynamic over at least two decades in temperature. Quadratic power-law behavior of both spin-lattice relaxation rate and specific heat indicates gapless nature of the ground state. We argue that this exotic behavior may be related to an unprecedented combination of the triangular and honeycomb geometries of nearest-neighbor exchange couplings.

Frustrated magnets host an exotic state called quantum spin liquid (QSL). In a QSL, spins are strongly correlated, but quantum fluctuations prevent them from long-range ordering [1, 2]. The initial (and subsequently rebutted) proposal of the QSL resonating-valence-bond state on the triangular lattice of Heisenberg spins [3] was followed by several other isotropic (Heisenberg) spin- $\frac{1}{2}$ models, where the formation of QSLs is now established [4–7]. A few candidate QSL materials proposed over the last decade bear key experimental signatures of this exotic state, including persistent spin dynamics and the absence of long-range order within the experimentally accessible temperature range [8–11].

Kitaev model with anisotropic interactions on the honeycomb lattice [12] offers an exact solution for the QSL state and expands the grounds for the QSL search from purely isotropic models to systems with strong magnetic anisotropy. Although no real-world material prototype of the Kitaev model has been reported to date, Ir^{4+} and Ru^{3+} compounds with the honeycomb interaction geometry show signatures of the Kitaev physics [13–16], despite the fact that at low temperatures long-range order sets in. The $4f$ compounds open another venue for the QSL physics [17, 18]. However, weak yet pertinent structural disorder is integral to many of the $4f$ materials reported to date [19–22].

In this Letter, we present the mixed-valence iridate $\text{Ba}_3\text{InIr}_2\text{O}_9$ as a structurally perfect QSL candidate with the $5d$ $\text{Ir}^{4.5+}$ ions. We confirm persistent spin dynamics and the absence of long-range magnetic order down to at least 20 mK and further identify quadratic power-law behavior of both specific heat and spin-lattice relaxation rate, which, in turn, indicates a gapless QSL state and is

highly uncommon for QSL materials.

$\text{Ba}_3\text{InIr}_2\text{O}_9$ belongs to the family of 6H-BaTiO_3 -type oxides $\text{A}_3\text{BM}_2\text{O}_9$. Their structures comprise single BO_6 octahedra and M_2O_9 dimers of two face-sharing MO_6 octahedra (Fig. 1a). When magnetic ion occupies the B site, triangular interaction geometry is formed, as in $\text{Ba}_3\text{CoSb}_2\text{O}_9$, which is arguably the best model spin- $\frac{1}{2}$ antiferromagnet on the triangular lattice [23–25]. Placing a $4d$ or $5d$ ion into the B site or into one of the M sites could give rise to a triangular system with strong Kitaev interactions [26, 27], but experimental implementation of this idea is hindered by the strong B/M site mixing that occurs, e.g., in $\text{Ba}_3\text{IrTi}_2\text{O}_9$ [28, 29]. Alternatively, Ir could be introduced into both M sites, while keeping the B site non-magnetic, but for integer valence of M the dimer would simply condense into a non-magnetic singlet [30, 31]. Mixed-valence systems with both M sites occupied by a magnetic $5d$ ion are possible too [32–35], and seem to be more promising for finding a QSL, because unpaired electrons that do not form singlets appear.

Guided by this idea, we synthesized $\text{Ba}_3\text{InIr}_2\text{O}_9$ in the polycrystalline form by a solid-state reaction method [33, 36]. Rietveld refinement of room-temperature neutron diffraction data (Fig. 1d) confirms hexagonal crystal structure ($P6_3/mmc$) and excludes any In/Ir site mixing [36], thus rendering $\text{Ba}_3\text{InIr}_2\text{O}_9$ a structurally perfect material. All Ir atoms occupy the same crystallographic position suggesting the true mixed-valence $\text{Ir}^{4.5+}$ state.

Thermodynamic properties of $\text{Ba}_3\text{InIr}_2\text{O}_9$ were studied using commercial MPMS and PPMS from Quantum Design. Temperature dependence of the magnetic susceptibility ($\chi = M/H$) measured in various applied fields

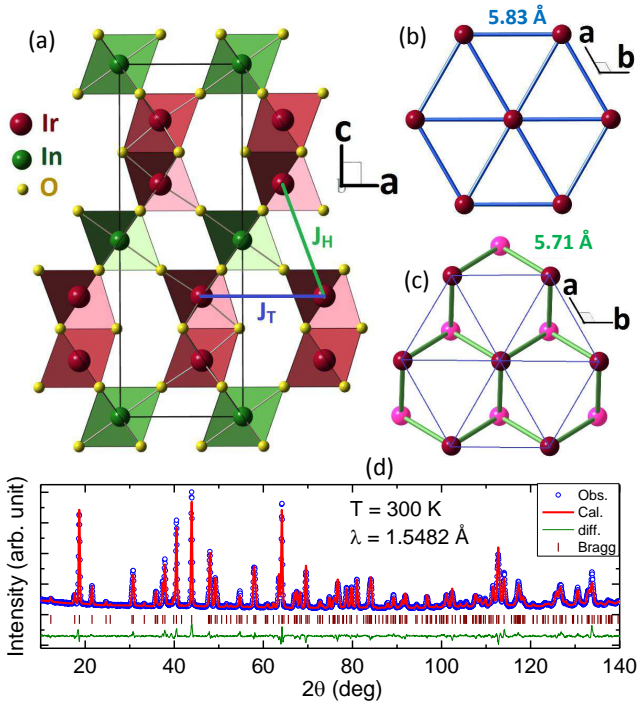


FIG. 1. (a) The crystal structure of $\text{Ba}_3\text{InIr}_2\text{O}_9$ comprising the IrO_6 and InO_6 octahedra shown in red and green colors, respectively. The Ba atoms are omitted for clarity. (b) The intra-plane coupling J_T forming the triangular lattice. (c) The interplane coupling J_H forming the honeycomb lattice. (d) Room-temperature Rietveld refinement of neutron diffraction data [36].

is shown in Fig. 2a. Down to 2 K, we did not observe any anomaly or divergence of field-cooled and zero-field-cooled data, suggesting the absence of long-range ordering and spin freezing.

Inverse susceptibility is linear between 10 and 70 K. Deviations from the Curie-Weiss (CW) behavior at higher temperatures [36] are possibly due to thermal changes in the Ir_2O_9 dimers that can adopt different competing electronic states [37]. Detailed investigation of this high-temperature behavior goes beyond the scope of the present work, where we focus on the low-temperature regime with the paramagnetic effective moment of $\mu_{\text{eff}} = 0.7 \mu_B/\text{dimer}$ extracted from the CW fit. This moment is lower than $1.73 \mu_B/\text{dimer}$ expected for one electron shared between the two $\text{Ir}^{4.5+}$ ions, but it seems plausible that the spin-orbit coupling reduces the moment considerably [37]. Indeed, in other mixed-valence iridates similar effective moments of less than $1 \mu_B/\text{f.u.}$ were reported [38, 39].

In $\text{Ba}_3\text{InIr}_2\text{O}_9$, local moments are coupled antiferromagnetically, as confirmed by the negative Curie-Weiss temperature $\theta_\chi = -7$ K. This energy scale of the interactions is in agreement with the specific heat (C_p), where a broad peak in C_p/T is observed around 1.6 K (Fig. 2b)

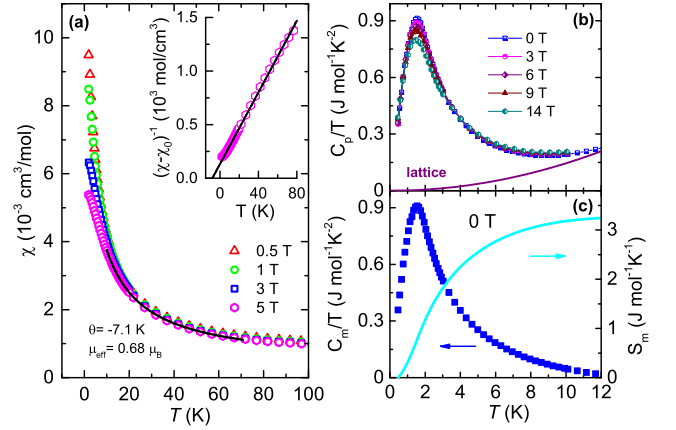


FIG. 2. (a) Magnetic susceptibility of $\text{Ba}_3\text{InIr}_2\text{O}_9$ shown as function of temperature at various applied fields. The Curie-Weiss fit of the 5 T data is shown as the black solid line. Inset: inverse 5 T susceptibility along with the CW fit. (b) Temperature dependence of C_p/T at various fields together with the lattice contribution. (c) For zero-field data, the temperature dependence of the magnetic heat capacity divided by temperature (C_m/T) and the entropy change (S_m) are also shown corresponding to the left and right axes, respectively.

indicative of a crossover between the paramagnetic (thermally disordered) and spin-liquid (quantum disordered) regimes [40, 41]. The peak shifts toward lower temperatures in the applied field, although the changes are relatively minor even at 14 T, and no transition anomaly is observed.

For an insulating material, total heat capacity is a sum of the magnetic and lattice parts, $C_p = C_m + C_{\text{lat}}$. In the absence of a suitable non-magnetic analog, we fitted C_p data with βT^3 in the temperature range 14 – 20 K. The fitted curve is then extrapolated to lower temperatures and subtracted from the experimental data to obtain the magnetic contribution [36]. The fitting of the lattice part yields $\beta = 1.45 \text{ mJ mol}^{-1} \text{ K}^{-4}$ and the Debye temperature $\Theta_D = 272$ K. Zero-field C_m/T is shown as function of T in Fig. 2c. Below the peak at 1.6 K, it follows the power law, $C_m = \gamma T^\alpha$, with $\gamma = 770 \text{ mJ mol}^{-1} \text{ K}^{-2}$ and $\alpha = 2$ [36]. Quadratic behavior of the specific heat is relatively uncommon for QSL candidates and gives first indication of a gapless ground state, because otherwise low-energy excitations over a spin gap would give rise to the exponential decay of C_m at low temperatures.

By integrating C_m/T within the temperature range from 0.4 to 10 K, we estimated magnetic entropy of $3.26 \text{ J mol}^{-1} \text{ K}^{-1}$, which is about 57% of the entropy expected for $\text{spin-}\frac{1}{2}$. Part of the magnetic entropy should be then released at higher temperatures, where the magnetic contribution is concealed behind a much larger lattice term. We note here that a two-step release of the

magnetic entropy (and, consequently, two well-separated peaks of the magnetic specific heat C_m) are indeed expected in frustrated magnets [42, 43].

Whereas thermodynamic measurements provide first hints towards the absence of long-range magnetic order in $\text{Ba}_3\text{InIr}_2\text{O}_9$, experimental evidence for the QSL formation is not complete without a local probe. To this end, we use muon spin relaxation (μSR), which is a very sensitive technique to detect static local fields arising from weak long-range order or spin freezing. The μSR experiments were performed on the Dolly and LTF spectrometers at the Paul Scherrer Institute (PSI, Switzerland).

In Fig. 3a, the muon polarization at 20 mK is shown. The absence of oscillations in the zero-field (ZF) signal and the lack of the polarization recovery to $1/3$ indicate the absence of any frozen moments in $\text{Ba}_3\text{InIr}_2\text{O}_9$. The ZF μ^+ relaxation rate (λ_{ZF}) is estimated by fitting the ZF muon depolarization curves in the entire temperature range from 20 K down to 20 mK (see [36]). The estimated λ_{ZF} is shown as function of temperature in Fig. 3b. At high temperatures (20 K to 3 K), λ_{ZF} remains constant at $\sim 0.12 \mu\text{s}^{-1}$, which is consistent with the paramagnetic fluctuations of Ir moments according to the Bloembergen Purcell and Pound theory [44].

From 3 K down to 1 K, λ_{ZF} increases with decreasing temperature. The enhancement of λ_{ZF} in a narrow temperature window indicates a slowing down of Ir spin fluctuations due to the development of strong short-range correlations, a common feature seen in other QSL candidates [9, 10, 41]. The temperature range of this feature is fully consistent with the peak in the magnetic specific heat (Fig. 2b). Upon further cooling, λ_{ZF} shows temperature-independent behavior between 1 K and 20 mK.

In order to identify the origin of the depolarization rate, we performed decoupling experiments at 250 mK (shown in Fig. 3a) applying longitudinal fields (LF) from 5 mT up to 100 mT. Should the low-temperature plateau in λ_{ZF} arise from a static field, the size of this field can be estimated as $B_{\text{loc}} = \lambda/\gamma_\mu \approx 1.4 \text{ mT}$, where $\gamma_\mu = 135.5 \times 2\pi \text{ s}^{-1} \mu\text{T}^{-1}$ is the gyromagnetic ratio for muons. The static field can then be decoupled by applying an external magnetic field $\simeq 14 \text{ mT}$, which is one order magnitude higher than B_{loc} . The polarization curve under a field of 100 mT does not show the signs of a full polarization, suggesting that the plateau does not originate from a static internal field. Hence, the spins are dynamic in nature even at the lowest temperature of 20 mK, as expected in a QSL. The plateau-like behavior of λ_{ZF} toward lowest temperature indicates much slower spin dynamics of the material compared to the μSR time window and turns out as another characteristics of QSL candidates [9, 10, 41].

Nuclear magnetic resonance (NMR) is a concurrent probe for local magnetic fields and spin dynamics. We performed ^{115}In (nuclear spin $I = 9/2$) NMR using home-

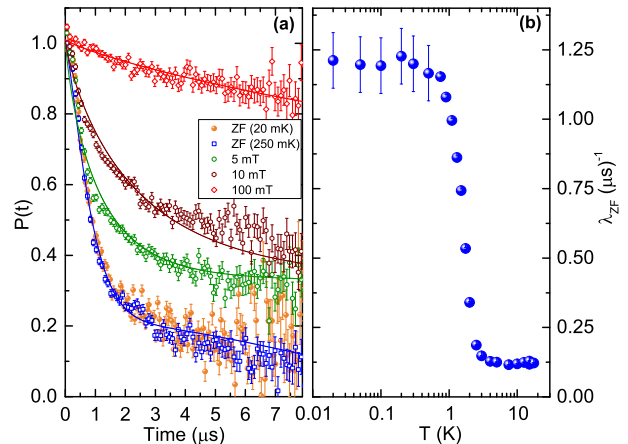


FIG. 3. (a) Muon polarization curve at 20 mK at zero field and at 250 mK with various applied magnetic fields are shown along with their fitting (see text). (b) Temperature dependence of λ_{ZF} at zero applied magnetic field.

built spectrometer with the dilution-fridge insert. The 70 MHz ^{115}In NMR spectrum at 138 K is shown in the inset of Fig. 4a. A single isotropic line indicates the unique crystallographic site for indium, which is consistent with our structural analysis [45]. The spectra can be described satisfactorily assuming the $I = 9/2$ nuclei with the 380 kHz quadrupolar coupling constant (ν_Q).

The spectra shift toward higher fields upon cooling, following the intrinsic spin susceptibility K of the material [36]. In general,

$$K = K_0 + (A_{\text{hf}}/N_A\mu_B)\chi(T), \quad (1)$$

where K_0 is the temperature-independent part of the line shift K , and N_A is the Avogadro's number. The hyperfine coupling constant is estimated at $A_{\text{hf}} = -1.675 \text{ T}/\mu_B$ [36]. The temperature dependence of the ^{115}In line shift (K) is shown in Fig. 4a. A continuous increase in the line shift $K(T)$ with decreasing temperature from 100 K down to $\sim 4 \text{ K}$ indicates the development of spin correlations. The inverse of the temperature-dependent part of the line shift $1/(K - K_0)$ is shown as a function of temperature in the inset of Fig. 4a. A CW fit of the data yields the CW temperature $\theta_{\text{NMR}} = -14 \text{ K}$. This value should be more reliable than $\theta_\chi = -7 \text{ K}$ estimated from the bulk susceptibility, since the NMR line shift does not contain any impurity contributions.

Below about 4 K, both the line shift K and line width ΔH (see Ref. [36]) of the spectra remain constant down to the base temperature of 25 mK. Saturation of both these quantities indicates that spin correlations are saturated below $\sim 4 \text{ K}$. The finite and temperature-independent value of K below 4 K gives strong evidence for the gapless behavior. From ΔH , we estimated the saturated mag-

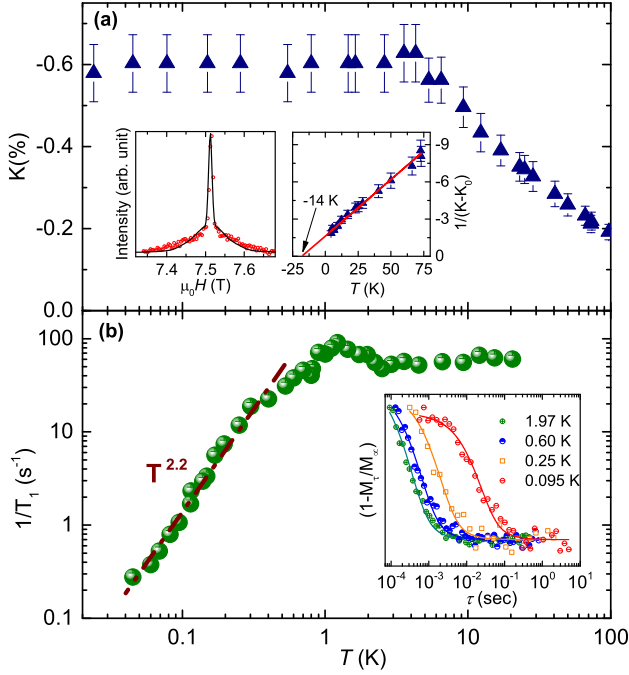


FIG. 4. (a) Temperature dependence of the line shift ^{115}K . Inset: (left) ^{115}In NMR spectrum at 138 K measured at 70 MHz along with its theoretical fit (see text), and (right) $1/(K - K_0)$ as function of temperature with the linear CW fit. (b) Temperature dependence of $1/T_1$. The dashed line is a guide-to-the-eye for the power-law $\propto T^{2.2}$ behavior. The inset shows the nuclear magnetization recoveries at different temperatures.

netic moment $\mu_s = 0.89 \mu_B/\text{f.u.}$ close to $1 \mu_B$ expected for one unpaired electron per the Ir_2O_9 dimer.

The NMR spin-lattice relaxation rate ($1/T_1$) probes low-energy spin dynamics. $1/T_1$ at different temperatures are obtained by fitting the longitudinal nuclear magnetization recovery curves as shown in the inset of Fig. 4b. In general,

$$(1/T_1 T) \sim \sum_q A_{\text{hf}}(q)^2 \times \chi''(q, \omega \rightarrow 0), \quad (2)$$

where $\chi''(q, \omega)$ is the imaginary part of the dynamical spin susceptibility. The temperature dependence of $1/T_1$ is shown in Fig. 4b. Between 30 K and 4 K, $1/T_1$ is almost temperature-independent, indicating the paramagnetic behavior. A weak hump-like feature is seen around 1.6 K, which coincides with the hump in the C_p/T data (Fig. 2b) and with the rapid increase in λ_{ZF} (Fig. 3b). No long-range order occurs in $\text{Ba}_3\text{InIr}_2\text{O}_9$. Therefore, this hump is not a broadened signature of a magnetic transition. Instead, it may indicate some intrinsic physics, as recently proposed for the Kitaev honeycomb iridates [46]. The applicability of this scenario to $\text{Ba}_3\text{InIr}_2\text{O}_9$ may be an interesting venue for future research.

More strikingly, $1/T_1$ follows the $\sim T^{2.2}$ power law at low temperatures in agreement with the quadratic behavior of $C_m(T)$. Theoretical concepts of gapless QSLs typically revolve around the idea of a spinon Fermi surface that would give rise to the linear behavior of both spin-lattice relaxation rate and magnetic specific heat [47–49] at low temperatures. Our data for $\text{Ba}_3\text{InIr}_2\text{O}_9$ clearly deviate from this scenario.

Contemplating the possible origin of this exotic behavior, we analyze the crystal structure of $\text{Ba}_3\text{InIr}_2\text{O}_9$. Assuming magnetic moments localized on the Ir_2O_9 dimers, two nearest-neighbor interactions may occur following the $\text{Ir}-\text{O}\dots\text{O}-\text{Ir}$ pathways. The intraplane interaction J_T (the $\text{Ir}-\text{Ir}$ distance of 5.83 Å) forms a triangular lattice in the ab plane (Fig. 1b). In contrast, the interplane interaction J_H (the $\text{Ir}-\text{Ir}$ distance of 5.71 Å) gives rise to honeycombs (Fig. 1c). Depending on the ratio between J_T and J_H , the system can interpolate between the purely two-dimensional regime ($|J_T| \gg |J_H|$, or vice versa) and a 3D behavior when both $|J_H|$ and $|J_T|$ are of the same size.

On the phenomenological level, quadratic behavior of the zero-field specific heat is expected in an algebraic spin liquid on the kagome lattice [50, 51]. Another manifestation of the T^2 behavior was proposed for a spin model combining the triangular and honeycomb geometries [52], as in $\text{Ba}_3\text{InIr}_2\text{O}_9$, but its applicability to our system is obscured by the large single-ion anisotropy term that is central to the model but seems unlikely in iridates. On the other hand, intersite anisotropies reminiscent of the Kitaev model may well be present. Intriguingly, the robust quadratic behavior of the zero-field specific heat has been reported in frustrated magnets with slow dynamics [53, 54] and interpreted in the framework of Halperin-Saslow modes for two-dimensional spin glasses [55, 56]. It was also observed in Li_2RhO_3 , Kitaev antiferromagnet with spin freezing [57]. To what extent these scenarios apply to $\text{Ba}_3\text{InIr}_2\text{O}_9$ with its persistent spin dynamics should be a subject of future investigations.

Altogether, we demonstrated that $\text{Ba}_3\text{InIr}_2\text{O}_9$ is a structurally perfect QSL candidate showing quadratic behavior of the specific heat and spin-lattice relaxation rate at low temperatures. Not only would it be interesting for further experimental (probe of the spin excitations with thermal conductivity and THz spectroscopy) and theoretical (microscopic analysis of the magnetic model) research, it also puts forward mixed-valence iridates as a promising playground for finding new QSL materials. The unique combination of the triangular and honeycomb geometries bears strong connections to current theoretical models of frustrated magnetism [12, 26, 58–61], and may lead to novel manifestations of the QSL physics when different lattice geometries concur.

We gratefully acknowledge financial support from the Deutsche Forschungsgemeinschaft (DFG) within the collaborative research center TRR 80 (Augs-

burg/Munich). TD, MM, and AT were funded by the Federal Ministry for Education and Research through the Sofja Kovalevskaya Award of Alexander von Humboldt Foundation. We thank C. Baines for his support on LTF.

* Email: tusdey@gmail.com

† Email: altsirlin@gmail.com

‡ Email: philipp.gegenwart@physik.uni-augsburg.de

- [1] L. Balents, “Spin liquids in frustrated magnets,” *Nature* **464**, 199–208 (2010).
- [2] L. Savary and L. Balents, “Quantum spin liquids: a review,” *Rep. Prog. Phys.* **80**, 016502 (2017).
- [3] P. W. Anderson, “Resonating valence bonds: A new kind of insulator?” *Mater. Res. Bull.* **8**, 153–160 (1973).
- [4] S. Yan, D. A. Huse, and S. R. White, “Spin-liquid ground state of the $S = 1/2$ kagome Heisenberg antiferromagnet,” *Science* **332**, 1173–1176 (2011).
- [5] R. Kaneko, S. Morita, and M. Imada, “Gapless spin-liquid phase in an extended spin-1/2 triangular Heisenberg model,” *J. Phys. Soc. Jpn.* **83**, 093707 (2014).
- [6] W.-J. Hu, S.-S. Gong, W. Zhu, and D. N. Sheng, “Competing spin-liquid states in the spin- $\frac{1}{2}$ Heisenberg model on the triangular lattice,” *Phys. Rev. B* **92**, 140403(R) (2015).
- [7] Y. Iqbal, W.-J. Hu, R. Thomale, D. Poilblanc, and F. Becca, “Spin liquid nature in the Heisenberg $J_1 - J_2$ triangular antiferromagnet,” *Phys. Rev. B* **93**, 144411 (2016).
- [8] M. R. Norman, “Colloquium: Herbertsmithite and the search for the quantum spin liquid,” *Rev. Mod. Phys.* **88**, 041002 (2016).
- [9] B. Fåk, E. Kermarrec, L. Messio, B. Bernu, C. Lhuillier, F. Bert, P. Mendels, B. Koteswararao, F. Bouquet, J. Ollivier, A. D. Hillier, A. Amato, R. H. Colman, and A. S. Wills, “Kapellasite: A kagome quantum spin liquid with competing interactions,” *Phys. Rev. Lett.* **109**, 037208 (2012).
- [10] L. Clark, J. C. Orain, F. Bert, M. A. De Vries, F. H. Aidoudi, R. E. Morris, P. Lightfoot, J. S. Lord, M. T. F. Telling, P. Bonville, J. P. Attfield, P. Mendels, and A. Harrison, “Gapless spin liquid ground state in the $S = \frac{1}{2}$ vanadium oxyfluoride kagome antiferromagnet $[\text{NH}_4]_2[\text{C}_7\text{H}_{14}\text{N}][\text{V}_7\text{O}_6\text{F}_{18}]$,” *Phys. Rev. Lett.* **110**, 207208 (2013).
- [11] C. Balz, B. Lake, J. Reuther, H. Luetkens, R. Schönemann, T. Herrmannsdörfer, Y. Singh, A. T. M. Nazmul Islam, E. M. Wheeler, J. A. Rodriguez-Rivera, T. Guidi, G. G. Simeoni, C. Baines, and H. Ryll, “Physical realization of a quantum spin liquid based on a complex frustration mechanism,” *Nature Phys.* **12**, 942–949 (2016).
- [12] A. Kitaev, “Anyons in an exactly solved model and beyond,” *Ann. Phys.* **321**, 2–111 (2006).
- [13] G. Jackeli and G. Khaliullin, “Mott insulators in the strong spin-orbit coupling limit: From Heisenberg to a quantum compass and Kitaev models,” *Phys. Rev. Lett.* **102**, 017205 (2009).
- [14] J. Nasu, J. Knolle, D. L. Kovrizhin, Y. Motome, and R. Moessner, “Fermionic response from fractionalization in an insulating two-dimensional magnet,” *Nature Phys.* **12**, 912–915 (2016).
- [15] A. Banerjee, C. A. Bridges, J.-Q. Yan, A. A. Aczel, L. Li, M. B. Stone, G. E. Granroth, M. D. Lumsden, Y. Yiu, J. Knolle, S. Bhattacharjee, D. L. Kovrizhin, R. Moessner, D. A. Tennant, D. G. Mandrus, and S. E. Nagler, “Proximate Kitaev quantum spin liquid behaviour in a honeycomb magnet,” *Nature Mater.* **15**, 733–740 (2016).
- [16] S. Trebst, “Kitaev materials,” *arXiv:1701.07056*.
- [17] L. Savary and L. Balents, “Coulombic quantum liquids in spin-1/2 pyrochlores,” *Phys. Rev. Lett.* **108**, 037202 (2012).
- [18] M. J. P. Gingras and P. A. McClarty, “Quantum spin ice: a search for gapless quantum spin liquids in pyrochlore magnets,” *Rep. Prog. Phys.* **77**, 056501 (2014).
- [19] A. Yaouanc, P. Dalmass de Réotier, C. Marin, and V. Glazkov, “Single-crystal versus polycrystalline samples of magnetically frustrated $\text{Yb}_2\text{Ti}_2\text{O}_7$: Specific heat results,” *Phys. Rev. B* **84**, 172408 (2011).
- [20] K. A. Ross, Th. Proffen, H. A. Dabkowska, J. A. Quillian, L. R. Yaraskavitch, J. B. Kycia, and B. D. Gaulin, “Lightly stuffed pyrochlore structure of single-crystalline $\text{Yb}_2\text{Ti}_2\text{O}_7$ grown by the optical floating zone technique,” *Phys. Rev. B* **86**, 174424 (2012).
- [21] Y. Li, D. Adroja, R. I. Bewley, D. Voneshen, A. A. Tsirlin, P. Gegenwart, and Q. Zhang, “Crystalline electric field randomness in the triangular lattice spin-liquid YbMgGaO_4 ,” *arXiv:1701.07056*.
- [22] J. A. M. Paddison, M. Daum, Z. Dun, G. Ehlers, Y. Liu, M. B. Stone, H. Zhou, and M. Mourigal, “Continuous excitations of the triangular-lattice quantum spin liquid YbMgGaO_4 ,” *Nature Phys.* **113**, 117–122 (2017).
- [23] Y. Shirata, H. Tanaka, A. Matsuo, and K. Kindo, “Experimental realization of a spin-1/2 triangular-lattice Heisenberg antiferromagnet,” *Phys. Rev. Lett.* **108**, 057205 (2012).
- [24] H. D. Zhou, C. Xu, A. M. Hallas, H. J. Silverstein, C. R. Wiebe, I. Umegaki, J. Q. Yan, T. P. Murphy, J.-H. Park, Y. Qiu, J. R. D. Copley, J. S. Gardner, and Y. Takano, “Successive phase transitions and extended spin-excitation continuum in the $S = \frac{1}{2}$ triangular-lattice antiferromagnet $\text{Ba}_3\text{CoSb}_2\text{O}_9$,” *Phys. Rev. Lett.* **109**, 267206 (2012).
- [25] J. Ma, Y. Kamiya, T. Hong, H. B. Cao, G. Ehlers, W. Tian, C. D. Batista, Z. L. Dun, H. D. Zhou, and M. Matsuda, “Static and dynamical properties of the spin-1/2 equilateral triangular-lattice antiferromagnet $\text{Ba}_3\text{CoSb}_2\text{O}_9$,” *Phys. Rev. Lett.* **116**, 087201 (2016).
- [26] M. Becker, M. Hermanns, B. Bauer, M. Garst, and S. Trebst, “Spin-orbit physics of $j = \frac{1}{2}$ Mott insulators on the triangular lattice,” *Phys. Rev. B* **91**, 155135 (2015).
- [27] A. Catuneanu, J. G. Rau, H.-S. Kim, and H.-Y. Kee, “Magnetic orders proximal to the Kitaev limit in frustrated triangular systems: Application to $\text{Ba}_3\text{IrTi}_2\text{O}_9$,” *Phys. Rev. B* **92**, 165108 (2015).
- [28] T. Dey, A. V. Mahajan, P. Khuntia, M. Baenitz, B. Koteswararao, and F. C. Chou, “Spin-liquid behavior in $J_{\text{eff}} = \frac{1}{2}$ triangular lattice compound $\text{Ba}_3\text{IrTi}_2\text{O}_9$,” *Phys. Rev. B* **86**, 140405(R) (2012).
- [29] R. Kumar, D. Sheptyakov, P. Khuntia, K. Rolfs, P. G. Freeman, H. M. Rønnow, T. Dey, M. Baenitz, and A. V. Mahajan, “ $\text{Ba}_3\text{M}_x\text{Ti}_{3-x}\text{O}_9$ ($\text{M} = \text{Ir}, \text{Rh}$): A family of $5d/4d$ -based diluted quantum spin liquids,” *Phys. Rev. B* **94**, 174410 (2016).
- [30] J. Darriet, M. Drillon, G. Villeneuve, and

- P. Hagenmuller, “Interactions magnétiques dans des groupements binucléaires du Ruthénium +V,” *J. Solid State Chem.* **19**, 213–220 (1976).
- [31] J. Darriet, J.L. Soubeyroux, and A.P. Murani, “Neutron inelastic scattering study of exchange interactions in a ruthenium(V) dimer $\text{Ba}_3\text{CaRu}_2\text{O}_9$,” *J. Phys. Chem. Solids* **44**, 269–272 (1983).
- [32] Y. Doi and Y. Hinatsu, “The structural and magnetic characterization of 6H-perovskite-type oxides $\text{Ba}_3\text{LnIr}_2\text{O}_9$ ($\text{Ln} = \text{Y}$, lanthanides),” *J. Phys.: Condens. Matter* **16**, 2849–2860 (2004).
- [33] T. Sakamoto, Y. Doi, and Y. Hinatsu, “Crystal structures and magnetic properties of 6H-perovskite-type oxides $\text{Ba}_3\text{MIr}_2\text{O}_9$ ($\text{M} = \text{Mg}$, Ca , Sc , Ti , Zn , Sr , Zr , Cd and In),” *J. Solid State Chem.* **179**, 2595–2601 (2006).
- [34] T. Dey, A. V. Mahajan, R. Kumar, B. Koteswararao, F. C. Chou, A. A. Omrani, and H. M. Ronnow, “Possible spin-orbit driven spin-liquid ground state in the double perovskite phase of $\text{Ba}_3\text{YIr}_2\text{O}_9$,” *Phys. Rev. B* **88**, 134425 (2013).
- [35] T. Dey, R. Kumar, A. V. Mahajan, S. D. Kaushik, and V. Siruguri, “Unconventional magnetism in the spin-orbit-driven Mott insulators $\text{Ba}_3\text{MIr}_2\text{O}_9$ ($\text{M} = \text{Sc}$, Y),” *Phys. Rev. B* **89**, 205101 (2014).
- [36] See Supplemental Material for details of synthesis, structure refinement, thermodynamic measurements, NMR, and μSR data.
- [37] S. V. Streltsov and D. I. Khomskii, “Covalent bonds against magnetism in transition metal compounds,” *Proc. Nat. Acad. Sci.* **113**, 10491–10496 (2016).
- [38] W. Müller, M. Avdeev, Q. Zhou, B. J. Kennedy, N. Sharma, R. Kutteh, G. J. Kearley, S. Schmid, K. S. Knight, P. E. R. Blanchard, and C. D. Ling, “Giant magnetoelastic effect at the opening of a spin-gap in $\text{Ba}_3\text{BiIr}_2\text{O}_9$,” *J. Amer. Chem. Soc.* **134**, 3265–3270 (2012).
- [39] J. Terzic, J. C. Wang, F. Ye, W. H. Song, S. J. Yuan, S. Aswartham, L. E. DeLong, S. V. Streltsov, D. I. Khomskii, and G. Cao, “Coexisting charge and magnetic orders in the dimer-chain iridate $\text{Ba}_5\text{AlIr}_2\text{O}_{11}$,” *Phys. Rev. B* **91**, 235147 (2015).
- [40] Y. Li, H. Liao, Z. Zhang, S. Li, F. Jin, L. Ling, L. Zhang, Y. Zou, L. Pi, Z. Yang, J. Wang, Z. Wu, and Q. Zhang, “Gapless quantum spin liquid ground state in the two-dimensional spin-1/2 triangular antiferromagnet YbMgGaO_4 ,” *Sci. Reports* **5**, 16419 (2015).
- [41] Y. Li, D. Adroja, P. K. Biswas, P. J. Baker, Q. Zhang, J. Liu, A. A. Tsirlin, P. Gegenwart, and Q. Zhang, “Muon spin relaxation evidence for the $\text{U}(1)$ quantum spin-liquid ground state in the triangular antiferromagnet YbMgGaO_4 ,” *Phys. Rev. Lett.* **117**, 097201 (2016).
- [42] P. Sindzingre, G. Misguich, C. Lhuillier, B. Bernu, L. Pierre, Ch. Waldtmann, and H.-U. Everts, “Magnetothermodynamics of the spin-1/2 kagomé antiferromagnet,” *Phys. Rev. Lett.* **84**, 2953–2956 (2000).
- [43] J. Nasu, M. Udagawa, and Y. Motome, “Thermal fractionalization of quantum spins in a Kitaev model: Temperature-linear specific heat and coherent transport of Majorana fermions,” *Phys. Rev. B* **92**, 115122 (2015).
- [44] N. Bloembergen, E. M. Purcell, and R. V. Pound, “Relaxation effects in nuclear magnetic resonance absorption,” *Phys. Rev.* **73**, 679 (1948).
- [45] Below 100 K, a second line with the temperature-independent Knight shift was observed. We ascribe this line to trace amounts of an impurity phase, see [36].
- [46] J. Yoshitake, J. Nasu, and Y. Motome, “Fractional spin fluctuations as a precursor of quantum spin liquids: Majorana dynamical mean-field study for the Kitaev model,” *Phys. Rev. Lett.* **117**, 157203 (2016).
- [47] M. J. Lawler, A. Paramakanti, Y. B. Kim, and L. Balents, “Gapless spin liquids on the three-dimensional hyperkagome lattice of $\text{Na}_4\text{Ir}_3\text{O}_8$,” *Phys. Rev. Lett.* **101**, 197202 (2008).
- [48] S. Yamashita, Y. Nakazawa, M. Oguni, Y. Oshima, H. Nojiri, Y. Shimizu, K. Miyagawa, and K. Kanoda, “Thermodynamic properties of a spin-1/2 spin-liquid state in a kappa-type organic salt,” *Nature Phys.* **4**, 459–462 (2008).
- [49] S. Yamashita, T. Yamamoto, Y. Nakazawa, M. Tamura, and R. Kato, “Gapless spin liquid of an organic triangular compound evidenced by thermodynamic measurements,” *Nature Comm.* **2**, 275 (2011).
- [50] Y. Ran, M. Hermele, P. A. Lee, and X.-G. Wen, “Projected-wave-function study of the spin-1/2 heisenberg model on the kagomé lattice,” *Phys. Rev. Lett.* **98**, 117205 (2007).
- [51] M. Hermele, Y. Ran, P. A. Lee, and X.-G. Wen, “Properties of an algebraic spin liquid on the kagome lattice,” *Phys. Rev. B* **77**, 224413 (2008).
- [52] G. Chen, M. Hermele, and L. Radzihovsky, “Frustrated quantum critical theory of putative spin-liquid phenomenology in 6H-B- $\text{Ba}_3\text{NiSb}_2\text{O}_9$,” *Phys. Rev. Lett.* **109**, 016402 (2012).
- [53] A. P. Ramirez, G. P. Espinosa, and A. S. Cooper, “Elementary excitations in a diluted antiferromagnetic kagomé lattice,” *Phys. Rev. B* **45**, 2505–2508 (1992).
- [54] S. Nakatsuji, Y. Nambu, H. Tonomura, O. Sakai, S. Jonas, C. Broholm, H. Tsunetsugu, Y. Qiu, and Y. Maeno, “Spin disorder on a triangular lattice,” *Science* **309**, 1697–1700 (2005).
- [55] S. Sachdev, “Kagomé- and triangular-lattice Heisenberg antiferromagnets: Ordering from quantum fluctuations and quantum-disordered ground states with unconfined bosonic spinons,” *Phys. Rev. B* **45**, 12377–12396 (1992).
- [56] D. Podolsky and Y. B. Kim, “Halperin-Saslow modes as the origin of the low-temperature anomaly in NiGa_2S_4 ,” *Phys. Rev. B* **79**, 140402(R) (2009).
- [57] P. Khuntia, S. Manni, F. R. Foronda, T. Lancaster, S. J. Blundell, P. Gegenwart, and M. Baenitz, “Local magnetism and spin dynamics of the frustrated honeycomb rhodate Li_2RhO_3 ,” arXiv:1512.04904.
- [58] I. Rousochatzakis, J. Reuther, R. Thomale, S. Rachel, and N. B. Perkins, “Phase diagram and quantum order by disorder in the Kitaev $K_1 - K_2$ honeycomb magnet,” *Phys. Rev. X* **5**, 041035 (2015).
- [59] G. Jackeli and A. Avella, “Quantum order by disorder in the Kitaev model on a triangular lattice,” *Phys. Rev. B* **92**, 184416 (2015).
- [60] K. Li, S.-L. Yu, and J.-X. Li, “Global phase diagram, possible chiral spin liquid, and topological superconductivity in the triangular Kitaev-Heisenberg model,” *New J. Phys.* **17**, 043032 (2015).
- [61] I. Rousochatzakis, U. K. Rössler, J. van den Brink, and M. Daghofer, “Kitaev anisotropy induces mesoscopic \mathbb{Z}_2 vortex crystals in frustrated hexagonal antiferromagnets,” *Phys. Rev. B* **93**, 104417 (2016).

Supplemental Material

Gapless quantum spin liquid ground state in mixed-valence iridate $\text{Ba}_3\text{InIr}_2\text{O}_9$

SAMPLE PREPARATION

Polycrystalline samples of $\text{Ba}_3\text{InIr}_2\text{O}_9$ were prepared by a conventional solid-state reaction method [1]. Stoichiometric amounts of high-purity BaCO_3 , In_2O_3 , and Ir metal powder were mixed thoroughly, pressed into pellets, and calcined at 900°C for 12 h. Further, the pellet was crushed into powder, mixed well, pelletized, and fired at 1300°C for 4 days with several intermediate grindings.

CRYSTAL STRUCTURE

Room-temperature neutron diffraction data were collected at the high-resolution instrument SPODI [2] at FRM-II (TU Munich) using the wavelength of 1.55 \AA . Jana2006 software [3] was used for structure refinement. Refined atomic positions are listed in Table S1.

TABLE S1. Refined atomic positions for $\text{Ba}_3\text{InIr}_2\text{O}_9$ at room temperature. The U_{iso} are isotropic atomic displacement parameters (in 10^{-2} \AA^2). Lattice parameters: $a = 5.8316(1) \text{ \AA}$, $c = 14.4877(4) \text{ \AA}$, $P6_3/mmc$, $R_I = 0.039$, $R_p = 0.051$.

		x/a	y/b	z/c	U_{iso}
Ba1	$2b$	0	0	0.25	1.3(1)
Ba2	$4f$	$\frac{1}{3}$	$\frac{2}{3}$	0.9103(2)	0.9(1)
In	$2a$	0	0	0	0.4(1)
Ir	$4f$	$\frac{1}{3}$	$\frac{2}{3}$	0.1590(1)	1.29(3)
O1	$6h$	0.4867(2)	0.5133(2)	0.25	1.40(5)
O2	$12k$	0.1715(2)	0.3430(4)	0.0841(1)	2.1(1)

THERMODYNAMIC PROPERTIES

Magnetization measurements were carried out in a Quantum Design 5 T SQUID magnetometer and in a Quantum Design PPMS 14 T in the temperature range 2 – 350 K. Heat capacity measurements were performed in a Quantum Design PPMS in the field range 0 – 14 T and temperature range 0.4 – 200 K.

We fitted susceptibility data in the temperature range 10 – 70 K with the Curie-Weiss (CW) formula $\chi(T) = \chi_0 + C/(T - \theta)$ where $\chi_0 = 3.69 \times 10^{-4} \text{ emu/mol}$, C , and θ are the temperature-independent susceptibility, Curie constant, and Curie-Weiss temperature, respectively. The fit is shown in Fig. 2(a) of the main paper. The susceptibility data at high (above 70 K) temperatures (shown in Fig. S2) can not be described with the

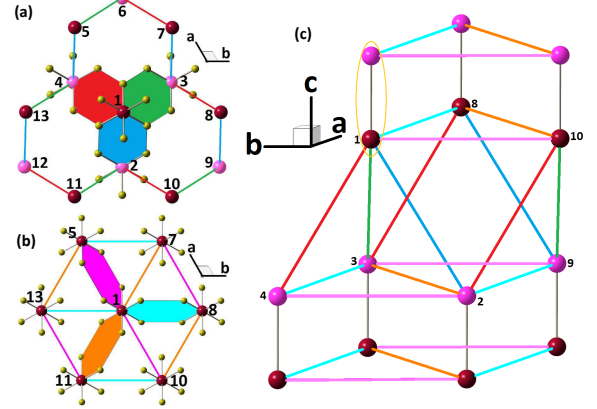


FIG. S1. (a) The honeycomb lattice formed by the coupling J_H . (b) The triangular lattice formed by the coupling J_T . (c) The honeycomb layer in between the two triangular layers is shown. The color code of the exchange pathways is same as in panels (a) and (b). The red and pink balls show Ir atoms from lower and upper sides of the dimer, respectively. Same numbering scheme for atoms is used. The yellow line encircles one dimer unit.

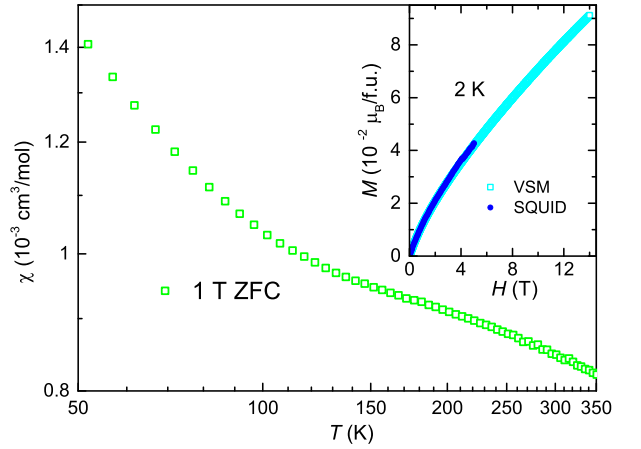


FIG. S2. Magnetic susceptibility of $\text{Ba}_3\text{InIr}_2\text{O}_9$ at 1 T is shown in the log-log scale in the temperature range 50–350 K. Insets: Isothermal magnetization curve measured at 2 K in SQUID (up to 5 T) and VSM (up to 14 T).

CW formula. Attempts to fit the data with the CW formula yield unreliable values, which strongly depend on the fitting range. The high $\theta = -310 \text{ K}$ obtained from fitting the susceptibility data above 200 K in Ref. [1] could be a result of similar problem.

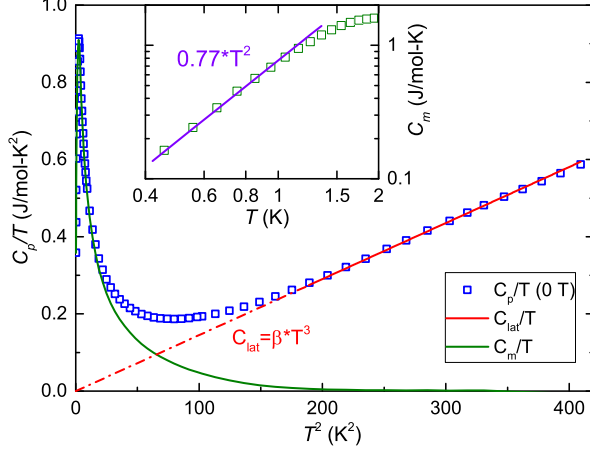


FIG. S3. C_p/T is shown as function of T^2 for the zero field data. The linear fit of the data in the range 14 – 20 K (red solid line) and its extrapolation down to low temperature (red dashed line) is shown. C_m/T obtained after subtracting the lattice part is shown as green solid line. Inset: The magnetic heat capacity is shown as function of temperature in log-log scale. The solid line is indicating quadratic temperature dependence.

To extract the magnetic specific heat of the material, we subtracted the lattice part from the total specific heat C_p . As shown in Fig. S3, we fitted the measured specific heat with $C_p = \beta T^3$ in the range 14 – 20 K. The fitted curve is extrapolated to lower temperatures and considered as the lattice part (C_{lat}). Further, we obtained the magnetic specific heat as $C_m = C_p - C_{\text{lat}}$, as shown on log scales in the inset. The estimated C_m follows the power law $C_m \propto T^2$ at low temperatures (cf. the inset of Fig. S3).

NMR MEASUREMENTS

^{115}In nuclear magnetic resonance (NMR) experiments were carried out with our home-built setup. The measurements are performed in the field-sweep mode at a fixed frequency of 70 MHz down to 24 mK. The spin echo intensity was obtained by integrating over the spin echo in the time domain. The final spectrum is constructed by plotting the spin-echo intensity as a function of the applied field.

NMR spectra measured at 70 MHz in the temperature range 0.024 – 135 K are shown in Fig. S4. At high temperatures, the spectra exhibit one single line. Below about 100 K we observed a new line which remains unshifted within the entire temperature range. This line presumably originates from a non-magnetic impurity phase present in the sample. The spectra are described

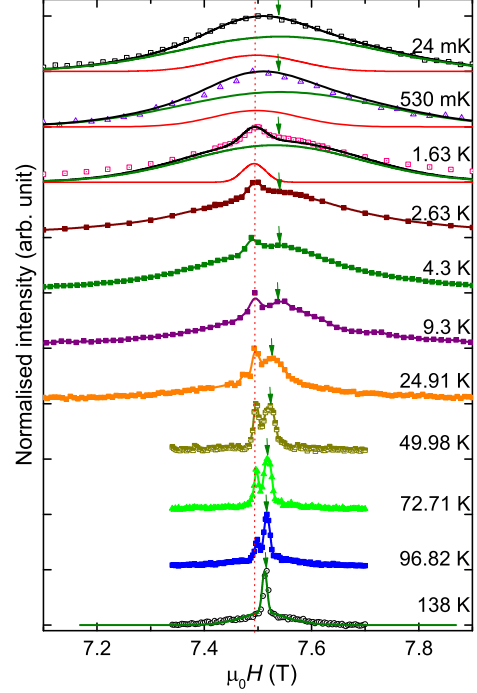


FIG. S4. Temperature evolution of NMR spectra measured at 70 MHz is shown. Individual spectra are shifted along y-axis for clarity. The vertical dotted red line indicates the diamagnetic resonance field as a reference. The spectra (black solid line) can be described well with the intrinsic (green solid line) and the non-magnetic impurity (red solid line) contribution, where the green arrow marks the peak position of the intrinsic line.

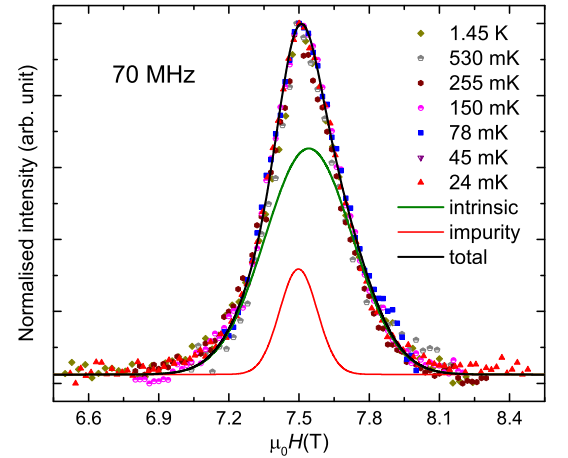


FIG. S5. Normalized ^{115}In NMR spectra at different temperatures between 1.45 K down to 24 mK. The green and red solid lines represent the intrinsic and impurity contributions, respectively, in the total spectra (black solid line) at 24 mK.

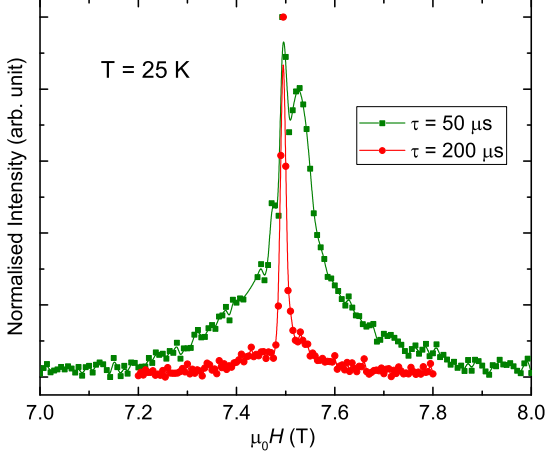


FIG. S6. NMR spectra measured with different pulse separation (τ) at 25 K.

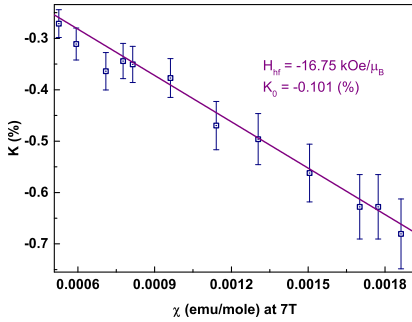


FIG. S7. Knight shift K versus susceptibility χ with temperature as an implicit parameter. The solid line is a linear fit.

at all temperatures below 100 K with two Gaussian lines, one for magnetic (intrinsic) and the other one for a non-magnetic (impurity) contribution. The peak of the majority contribution (intrinsic) shifts towards higher fields with decreasing temperature yielding the local spin susceptibility K (see the arrow in Fig. S4). At low temperatures, the two lines (intrinsic line and the impurity line) merge together. For estimating the Knight shift of the intrinsic line we have used the peak position of the green line S4.

In order to estimate the hyperfine coupling constant A_{hf} , we plotted $K(T)$ vs $\chi(T)$ (cf. to Fig. S7) with T as an implicit parameter. From the slope of the linear behavior, we estimate A_{hf} .

Figure S5 clearly shows that the total spectra remain unchanged (no shift and no broadening) from 1.45 K down to 24 mK. This indicates that the line width as

well as the shift of the intrinsic line are temperature-independent below 1.4 K.

For estimating the impurity contribution in the spectral line shape, we measured the spectra at a few temperatures with $\tau = 50 \mu\text{s}$ and $\tau = 200 \mu\text{s}$, where τ is the pulse separation between the spin-echo sequence $\pi/2 - \tau - \pi$. The intrinsic line has much shorter spin-lattice relaxation time T_1 as well as the spin-spin relaxation time T_2 compared to the impurity line. Hence it is expected that with longer τ the intrinsic part of the spectra is already relaxed, whereas the impurity contribution sustains. The comparison of the spectra corresponding to different τ measured at $T = 25 \text{ K}$ is shown in Fig. S6.

The spin-lattice relaxation rate ($1/T_1$) was measured at the peak position of the intrinsic line. Long pulses were used to avoid any interference from the impurity line. The rate $1/T_1$ at different temperatures has been determined by fitting the recovery curves with the equation

$$1 - M_t/M_\infty = C \left(0.006 e^{-(2Wt)^\beta} + 0.0335 e^{-(12Wt)^\beta} + 0.0925 e^{-(30Wt)^\beta} + 0.215 e^{-(56Wt)^\beta} + 0.653 e^{-(90Wt)^\beta} \right)$$

with $1/T_1 = 2W$. Here, M is the nuclear magnetization, β is a stretched exponent, which accounts for a distribution of the T_1 values due to disorder, and C is a pre-factor.

By solely exciting the impurity line, as documented in Fig. S6, we have measured the relaxation rate of the impurity line as a function of temperature (shown in Fig. S8). The relaxation rate of the impurity line decreases towards 10 K and remains constant at lower temperatures. The relaxation rate is much smaller compared to that of the intrinsic line at elevated temperatures ($T > 2 \text{ K}$). From the T_2 of the impurity line, we estimate the amount of the impurity at 0.9 %.

μSR MEASUREMENTS

The experiments were done on two different spectrometers at the Paul Scherrer Institute (Switzerland), LTF for temperatures from 20 mK up to 750 mK and Dolly for temperatures from 250 mK up to 20 K. For the Dolly experiment, about 300 mg of the polycrystalline sample was mounted on a thin copper plate inside the ^3He cryostat. In order to ensure good thermal contact, we glued the sample with GE varnish. We used the Veto mode, which allows to get rid of the background signal from the sample holder. Therefore, the acquired signal is due to muons that stopped inside the sample. For the LTF experiment we used the same sample, again glued with GE on a silver plate. By comparing the results obtained between 250 mK and 750 mK on both the spectrometers,

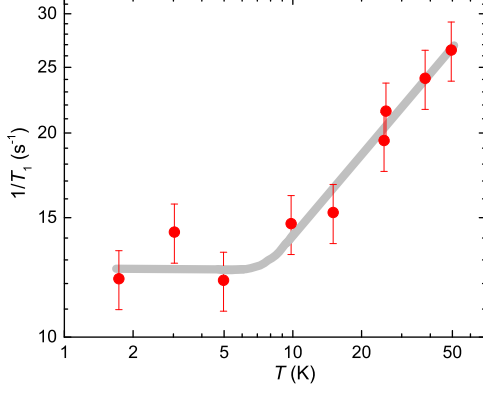


FIG. S8. Temperature dependence of $1/T_1$ for the non-magnetic impurity phase. The grey line is a guide to the eye.

we were able to get rid of the experimental background on LTF.

The relaxation curves of the muon polarization in ZF can be fitted in the whole temperature range from 20 K down to 20 mK by combining the depolarization due to the muon coupled to the In nuclear magnetism (Kubo-Toyabe Gaussian function) and depolarization due to the electronic magnetism, which evolves with temperature,

$$P(t) = f e^{-(\lambda_{ZF} t)^\beta} + (1-f) \left(\frac{1}{3} + \frac{2}{3} (1 - (\sigma t)^2) e^{-\frac{(\sigma t)^2}{2}} \right).$$

Here, $f = 0.786(2)$ is the fraction of muons coupled to the electronic magnetism, $\sigma = 0.094(2) \mu s^{-1}$ is the nuclear depolarization rate, $\beta = 1.308(7)$ is the stretched exponent, and λ is the electronic depolarization rate.

The plateau-like behavior in λ_{ZF} vs T (see Fig. 3b of the main paper) has also been observed in several other QSL compounds. Previous studies attributed such a behavior either to muons directly coupled to the frustrated lattice [4] or even to muons coupled to defects [5, 6]. By performing μ SR experiment under a transverse field (TF), one can estimate the μ SR line shift (K^μ) as a function of temperature, which can help to address this issue [7].

We performed the TF experiment in the field of 0.4 T. Temperature dependence of K^μ is depicted in Fig. S9. K^μ increases with decreasing temperature and saturates below 3 K, from where λ (see Fig. 3 (b) of the main paper) starts increasing. This indicates that antiferromagnetic (AFM) spin fluctuations are dominating at low temperature in $\text{Ba}_3\text{InIr}_2\text{O}_9$. The temperature variation of K^μ is very similar to the NMR shift ($K(\%)$) (see Fig. 4 (a) of the main paper). This proves that the muons are directly coupled to the Ir moments. Thus, the persistent spin dynamics probed by the ZF μ SR experiments is intrinsic

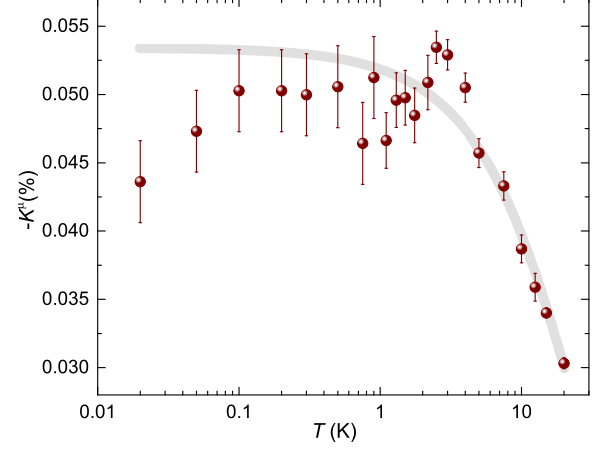


FIG. S9. μ SR shift ($-K^\mu$) measured in the applied transverse field 0.4 T as function of temperature.

to the frustrated lattice and further establishes the QSL ground state of $\text{Ba}_3\text{InIr}_2\text{O}_9$.

* Email: tusdey@gmail.com

† Email: altsirlin@gmail.com

‡ Email: philipp.gegenwart@physik.uni-augsburg.de

- [1] T. Sakamoto, Y. Doi, and Y. Hinatsu, "Crystal structures and magnetic properties of 6H-perovskite-type oxides $\text{Ba}_3\text{MIr}_2\text{O}_9$ (M = Mg, Ca, Sc, Ti, Zn, Sr, Zr, Cd and In)," *J. Solid State Chem.* **179**, 2595–2601 (2006).
- [2] M. Hoelzel, A. Senyshyn, N. Juenke, H. Boysen, W. Schmahl, and H. Fuess, "High-resolution neutron powder diffractometer SPODI at research reactor FRM II," *Nuclear Instruments & Methods in Physics Research, Section A: Accelerators, Spectrometers, Detectors, and Associated Equipment* **667**, 32–37 (2012).
- [3] V. Petříček, M. Dušek, and L. Palatinus, "Crystallographic computing system JANA2006: General features," *Z. Krist.* **229**, 345–352 (2014).
- [4] R. H. Colman, F. Bert, D. Boldrin, A. D. Hillier, P. Manuel, P. Mendels, and A. S. Wills, "Spin dynamics in the $S = 1/2$ quantum kagome compound vesignieite, $\text{Cu}_3\text{Ba}(\text{VO}_5\text{H})_2$," *Phys. Rev. B* **83**, 180416(R) (2011).
- [5] E. Kermarrec, P. Mendels, F. Bert, R. H. Colman, A. S. Wills, P. Strobel, P. Bonville, A. Hillier, and A. Amato, "Spin-liquid ground state in the frustrated kagome antiferromagnet $\text{MgCu}_3(\text{OH})_6\text{Cl}_2$," *Phys. Rev. B* **84**, 100401(R) (2011).
- [6] M. Gomilšek, M. Klanjšek, M. Pregelj, F. C. Coomer, H. Luetkens, O. Zaharko, T. Fennell, Y. Li, Q. M. Zhang, and A. Zorko, "Instabilities of spin-liquid states in a quantum kagome antiferromagnet," *Phys. Rev. B* **93**, 060405(R) (2016).
- [7] J. C. Orain, L. Clark, F. Bert, P. Mendels, P. Attfield, F. H. Aidoudi, R. E. Morris, P. Lightfoot, A. Amato, and

C. Baines, “ μ SR study of a quantum spin liquid candidate:

the $S = 1/2$ vanadium oxyfluoride kagome antiferromagnet,” J. Phys.: Conference Series **551**, 012004 (2014).